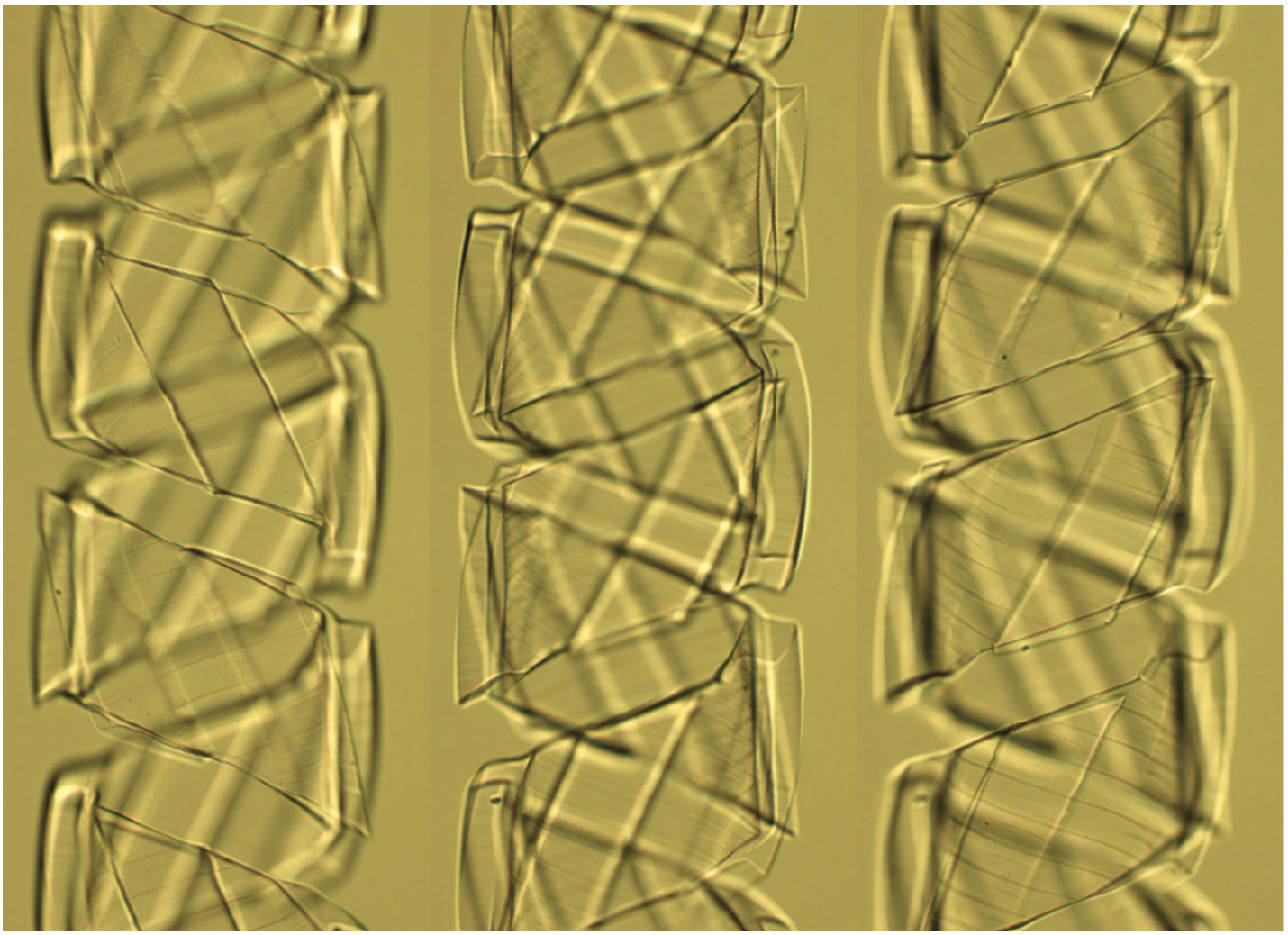

Highlighting Research from the University of Pennsylvania and Ulsan National Institute of Science and Technology.

Topography-guided buckling of swollen polymer bilayer films into three-dimensional structures

Based on physical constraints, simple surface topography can guide buckling of swollen polymer bilayer films and thereby control the morphology of resulting three-dimensional objects such as half-pipes, helical tubules, and ribbons.

As featured in:

See Joonwoo Jeong *et al.*, *Soft Matter*, 2017, **13**, 964.

ROYAL SOCIETY OF CHEMISTRY

rsc.li/soft-matter-journal

Registered charity number: 207890

Soft Matter

PAPER

Cite this: *Soft Matter*, 2017, **13**, 956

Topography-guided buckling of swollen polymer bilayer films into three-dimensional structures†

Joonwoo Jeong,‡*[ab] Yigil Cho,‡§[cd] Su Yeon Lee,‡[ce] Xingting Gong,[f] Randall D. Kamien,[d] Shu Yang[c] and A. G. Yodh[d]

Received 10th October 2016,
Accepted 23rd December 2016

DOI: 10.1039/c6sm02299e

www.rsc.org/softmatter

Thin films that exhibit spatially heterogeneous swelling often buckle into the third dimension to minimize stress. These effects, in turn, offer a promising strategy to fabricate complex three-dimensional structures from two-dimensional sheets. Here we employ surface topography as a new means to guide buckling of swollen polymer bilayer films and thereby control the morphology of resulting three-dimensional objects. Topographic patterns are created on poly(dimethylsiloxane) (PDMS) films selectively coated with a thin layer of non-swelling parylene on different sides of the patterned films. After swelling in an organic solvent, various structures are formed, including half-pipes, helical tubules, and ribbons. We demonstrate these effects and introduce a simple geometric model that qualitatively captures the relationship between surface topography and the resulting swollen film morphologies. The model's limitations are also examined.

Introduction

The elastic instabilities of thin two-dimensional (2D) sheets make possible new and promising strategies for building complex three-dimensional (3D) materials.[1–7] In essence, a small film thickness renders out-of-plane buckling easier than in-plane stretching because film-bending stiffness scales as thickness to the third power while film-stretching stiffness scales linearly with thickness.[7] From an engineering perspective these instabilities can produce wrinkling, creasing, global buckling, and delamination. Often, such effects are not desired for applications. However, inspired by paper folding techniques such as *origami* and *kirigami*, various groups have begun to develop new rules and material systems to harness mechanical instabilities and create complex functional 3D morphologies from pre-designed structured thin films.[6,8–23] The folding processes are often reversible, and the responsivity of the films to a variety of stimuli including temperature, pH, and light can be tuned for potential applications in sensing and actuation.[13,24–36] Such structures, however, can be expensive and challenging to fabricate using top-down methods such as lithography and layer-by-layer 3D printing.

Among the responsive materials that transform from 2D to 3D, polymer films are most studied because of their large deformability, their wide range of elastic moduli, and their solvent compatibility. Standard planar fabrication techniques such as photolithography and layer-by-layer assembly are commonly employed to program response in polymer films,[2,7,19,26,32,35,37–39] and multi-layer films consisting of polymers with different expansion/shrinkage responses are popular systems for this purpose.[19,37–39] Alternatively, single-layer polymer films with in-plane modulation of cross-linking density for non-uniform swelling/deswelling have also been demonstrated.[14,16,34,40] The starting film geometry for all of these methods is a 2D sheet with in-plane patterns that determine the final 3D film configurations. Surprisingly, in contrast to work on wrinkling and creasing,[41,42] most reports on global film buckling from 2D to 3D have not utilized surface topography – neither patterned thickness profiles nor selective coating of different materials on the patterns.

Here, we exploit the surface topography of a bilayer thin film to guide swelling-induced buckling behavior. To demonstrate this concept, we first create stripe patterns (by replica molding) with square-wave cross-sections on one-side of the swellable polymer, poly(dimethylsiloxane) (PDMS). Then a thin layer of non-swelling parylene was deposited uniformly and conformally onto the topographically-patterned side or the flat side of the

[a] *Department of Physics, Ulsan National Institute of Science and Technology (UNIST), Ulsan 44919, Republic of Korea. E-mail: jjeong@unist.ac.kr*
[b] *Center for Soft and Living Matter, Institute for Basic Science (IBS), Ulsan 44919, Republic of Korea*
[c] *Department of Materials Science and Engineering, University of Pennsylvania, 3231 Walnut Street, Philadelphia, PA 19104, USA*
[d] *Department of Physics and Astronomy, University of Pennsylvania, 209 South 33rd Street, Philadelphia, PA 19104, USA*
[e] *Division of Advanced Materials, Korea Research Institute of Chemical Technology (KRICT), Daejeon 34114, Republic of Korea*
[f] *Department of Applied Physics, Stanford University, Stanford, CA 94305, USA*
† Electronic supplementary information (ESI) available. See DOI: 10.1039/c6sm02299e
‡ Authors contributed equally to this work.
§ Present address: System Large-scale Integration (S.LSI) Division, Samsung Electronics, Yongin 17113, Republic of Korea.

PDMS film. After swelling in an organic solvent, the bilayer films exhibit global buckling because of mismatched swelling ratios between PDMS and parylene. We show that simple topographic patterning on the bilayer film can lead to various 3D structures, including half-pipes, helical tubules, and ribbons, based on a few physical constraints. Chiral structures are among the simplest naturally occurring model systems to study, and previous investigations have demonstrated fabrication of helical structures at the micro- and nano-scale by utilizing intrinsic chirality in their building blocks,[43,44] geometric asymmetry,[45] and stress within composite materials.[31,34,46–50] Our bilayer films also exploit internal stress after swelling, but the direction of buckling is guided by topography rather than the direction of pre-stretching[31,48–50] or in-plane modulation of swelling ratios[34] as previously demonstrated in literature. Our approach does not require sophisticated patterning techniques such as plasma etching or repeated photo-crosslinking with multiple masks.[14–16,19] Standard soft lithography is easily employed to create the topographic patterns. We expect that the topography method can be combined with other techniques, such as in-plane modulation of cross-linking density, to advance existing strategies.

To better understand the topographically controlled swelling behaviors, we introduce a simple geometric model and examine conditions for which more sophisticated modeling is required. The simple model qualitatively captures the resulting morphologies of our swollen films and provides a starting point for more sophisticated calculations. In essence, our geometric model uses constraints on the dimensions of a patterned bilayer film, before and after swelling, to predict final conformations. It finds the morphology that minimizes stretching/compression of the non-swelling parylene film and is consistent with expected swelling of the bilayer film, *e.g.*, that the stripe ridges align along the direction of zero principal curvature. Here, our model focuses on simple patterns such as stripes to first test validity of our approach; moreover, it is limited to situations where stretching/compression, and residual stress of parylene overlayer can be ignored and self-interactions within the buckled sheets are not important. Our model, despite simple, clearly shows that surface topography offers a simple yet rich means to guide elastic instability of films for creation of complex 3D objects.

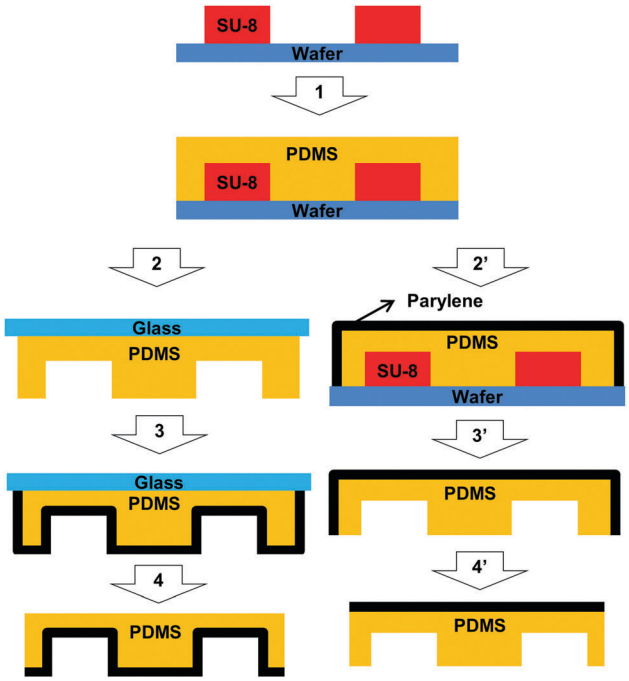

Fig. 1 Schematic for fabrication of topographically-patterned polymer bilayer films. PDMS (orange) is cured on a SU-8 mold (red) residing on top of a silicon wafer. Then a thin parylene film (black) is deposited *via* chemical vapor deposition onto either the topographically-patterned side (Step 3′) of the PDMS film or the flat side (Step 2′).

Materials and methods

Fabrication of topographically-patterned polymer bilayer films

As shown in Fig. 1, we employ two classes of topographic bilayer films for buckling. The topographic pattern is created by photolithography followed by replica molding of a soft elastomer, poly(dimethylsiloxane) (PDMS). Then a thin layer of non-swelling parylene-C is deposited onto the PDMS pattern, either on the back, flat side of the PDMS, or on the patterned side. In brief, a thin layer (50 μm thick) of negative photoresist SU-8 (Microchem Corp.) is spin-coated onto a silicon wafer, soft-baked at 95 °C for 7 min to remove the residual solvent, followed by UV curing (Hg lamp, wavelength of 365 nm, 200 mJ cm^{-2}) through a photomask. After exposure, the film is baked at 95 °C for 7 min and developed in propylene glycol methyl ether acetate (PGMEA, Sigma-Aldrich), followed by rinsing with isopropyl alcohol to generate the pattern.

In step 1, a mixture of PDMS precursor/crosslinker (10 : 1 weight ratio) is spin-coated onto the SU-8 topographic mold that was pre-treated by hexamethyldisilazane (HMDS) vapor for 30 min in order to facilitate the detachment of cured PDMS from the mold. Typically, a diced silicon wafer (25 25 mm) is fully covered by the PDMS mixture and then spun at rates between 1000 and 3000 rpm for 1 minute. The PDMS films are cured at 80 °C for 24 hours.

Parylene-C precursor dimer, dichloro-[2,2]-paracyclophane (0.5 g), is chemical vapor deposited (CVD) on PDMS using a commercial coater (PDS2010, Specialty Coating Systems, ~55 mTorr). Deposition onto the patterned PDMS film is carried out in two different ways. In approach I, parylene-C is conformally deposited on the topographically patterned side of the PDMS film. In approach II, parylene-C is deposited on the flat surface of the PDMS film (non-patterned side). The temperatures used for vaporization, pyrolysis, and deposition of parylene-C are 175 °C, 690 °C, and room temperature, respectively.

The bilayer films thus produced are cut into strips in their dry state. Fig. 2a shows two exemplary strips cut at different angles. The strips are produced by cutting the film with a razor blade. The width of the strip and the angle between the stripe pattern and the longitudinal direction of the strip are selected by this cutting process. Before swelling, the parylene-C film is 0.5–1 μm thick, and the PDMS film is ~100 μm thick. Note, the

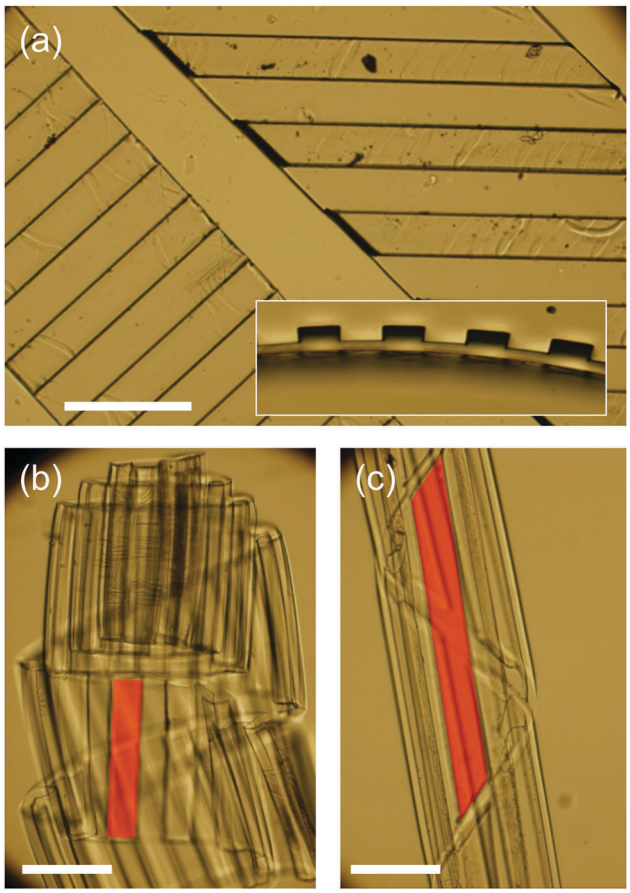

Fig. 2 Optical microscopy images of example strips of bilayer films with a thin layer of parylene-C film deposited on the topographically patterned side of the PDMS. Scale bars: 300 μm. (a) Top-view of two dry bilayer strips with ridges at different angles. (inset) Cross-sectional view of one dry bilayer strip showing the topographic pattern. (b and c) Swollen bilayer strips made from dry bilayer strips in (a); the strips are immersed in hexadecane. Note, the bottom-left strip of (a) transforms into (b) after swelling, and the top-right strip of (a) transforms into (c) after swelling. Red shading regions are provided to guide the eye about representative ridges on the strip.

approximate Young's moduli of parylene-C and PDMS are 3 GPa and 2 MPa, respectively.[51,52] The inset of Fig. 2a shows the square-wave cross-section of the resultant film; the thickness of the ridge with respect to the valley is ~50 μm and the distance from the valley to the flat bottom is ~25 μm.

Swelling and observation of polymer bilayer films

We placed these dry strips into a hexadecane solvent bath. A swelling ratio for unbounded PDMS in hexadecane has been reported as $\lambda = 1.14$;[53] in our experiments, however, we anticipate that the effective swelling ratio of the thin PDMS film bounded by parylene is likely to be smaller than the one reported for unbounded PDMS. The swelling ratio for parylene-C in hexadecane is negligible (in iso-octane it was measured to be 1.004). To observe strip swelling, the hexadecane bath is placed on a Leica DM IRB inverted microscope. In practice, we dip the strips gradually into the hexadecane from one end by taking hold of the other end with a tweezer. When the strips make a contact with the solvent, vigorous buckling occurs and finishes within a few seconds; thereafter, no further change in shape is observed. Due to these rapid motions, it is difficult to capture intermediate configurations during swelling. After the strips are completely immersed in hexadecane, we collect bright-field images of the swollen strips using either a 1.6 air objective with NA = 0.07 or a 10 air objective of NA = 0.25. Polychromatic illumination is derived from a halogen lamp. A color CCD camera (UC-1800DS-CL, UNIQ Vision Inc.) captured images of the samples.

The swollen strips can be de-swollen to recover initial flat configurations and then re-swollen to exhibit buckling again. For example, ethanol is a good de-swelling solvent because it is volatile, it is partially miscible with hexadecane, and it swells PDMS negligibly (see Fig. S1 in ESI†).

Results and discussion

We first investigate a simple case wherein the parylene-C thin film is deposited on the topographically-modulated side of the PDMS. Fig. 2 shows representative optical images of the dry and swollen bilayer films. Upon swelling, the strips buckle into helical ribbons with the flat side of the PDMS film located on the outside of the helical ribbon. Furthermore, the valleys and ridges of the topographical pattern align almost parallel to the helical axis of the ribbons. Thus the strip with the horizontal valleys and ridges evolves into tube-like ribbons. Note that this buckling behaviour is reproducible in the same batch and is reproducible even after repeated buckling of the same strip (see Fig. S2 and S3 in ESI†).

To build an analytic model for this process, we first define the important variables (see Fig. 3). In experiments, the width of the ridges (W_R) and the ridge valleys (W_V) are kept the same size, and the PDMS thicknesses in the valley and ridge regions are T_V (~25 μm) and T_R, respectively. The ratio T_V/T_R is approximately 0.33. We denote the length of the ridge (valley) as L_R (L_V). The valleys and ridges of the stripe patterns make an angle, α, with respect to the horizontal of the bilayer strip. Thus ridges and valleys perpendicular to the strip edge have $\alpha = 0^\circ$. Lastly, the bilayer films are cut into long strips of width W and length L, where $L \gg W$. Typically, the strip width ranges between 100 μm and a few millimeters. Fig. 3b shows 3D perspective views of the swollen structure and other variables. The non-swelling parylene-C film does not stretch and is intrinsically flat: its Gaussian curvature must vanish pointwise. Therefore, we can reasonably assume that the swollen structure is a helical ribbon with almost zero Gaussian curvature.

In this helical ribbon model, r is the distance between the helical axis and the flat side of the PDMS. Notice, we have implicitly assumed the strip globally buckles into a helical ribbon with a single radius r in spite of the thickness variation in the strip. We believe this assumption is reasonable because the ridges in Fig. 3 are surrounded by non-swelling parylene and thus show little swelling. Therefore, the radius is determined mainly by swelling of the region within T_V. As shown in

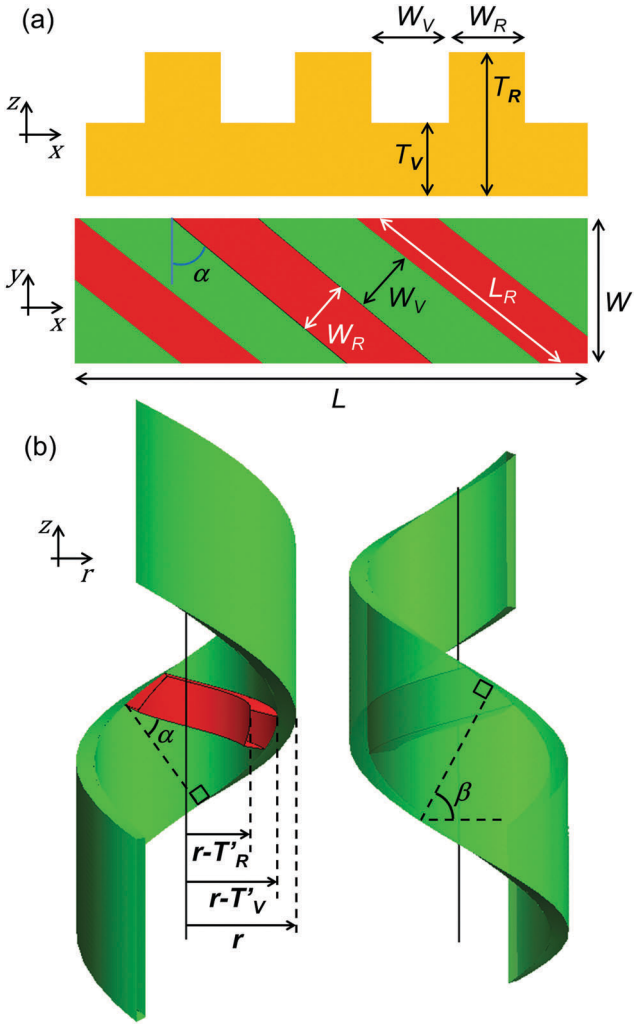

Fig. 3 Schematic model of the helical ribbon formation. (a) Cross-sectional view (top) and top-view (bottom) of the topographically patterned bilayer strip before swelling. The red and green regions correspond to ridges and valleys, respectively. W, W_R, W_V are the widths of the strip, ridge, and valley, respectively. T_R and T_V are thicknesses of the ridge and valley, respectively. L is the length of the strip, and α is the angle of the ridge with respect to the strip horizontal. (b) 3D perspective views of a helical ribbon after swelling. For clarity, only one representative ridge is shown. The straight black line along the z-axis is the helical axis. The radius, r, is the distance from the helical axis to the surface of the flat side of the PDMS film. T_R' and T_V' are thicknesses after swelling, and β is the angle of the ribbon with respect to the ribbon's circumferential direction.

Fig. 3b, subtracting T_V' (T_R') from r gives the distance between the helical axis and the valley (ridge) where T_X' represents thickness after swelling, *i.e.*, $T_X' = \lambda T_X$. β defines the pitch of the evolved helical structure, $2\pi r \cot\beta$; $\beta = 0$ degrees and $\beta = 90$ degrees correspond to the half pipe and tube structures, respectively. According to this definition of β, positive (negative) β corresponds to a left-handed (right-handed) helix.

The two parameters governing the shape of a helical ribbon, r and β, are determined by the swelling ratio of the PDMS in the solvent and the topographic pattern. We assume that the contour length of the PDMS film located outside of the helical ribbon, L_{out}, should be equal to λL, where λ is the effective swelling ratio:

$$L_{out} = L\sqrt{\sin^2\left(\frac{\pi}{2}-\beta\right) + \left(\frac{r}{r-T_V'}\cos\left(\frac{\pi}{2}-\beta\right)\right)^2} = \lambda L \quad (1)$$

The length of ridge (valley) in the swollen bilayer also depends on the parameters of the helical ribbon. The length of the ridge inside of the helical ribbon is

$$L_{R,in} = L_R\sqrt{\sin^2(\alpha-\beta) + \left(\frac{r-T_R'}{r-T_V'}\cos(\alpha-\beta)\right)^2} \quad (2)$$

Here, since $L_{R,in}$ is smaller than L_R, the parylene-C film covering the ridges will be compressed unless $\alpha - \beta = \pi/2$. This condition implies that the ridges must align parallel to the helical axis. In other words, the non-swelling thin film deposited on the topographic pattern guides buckling of the swollen film into a structure with minimal strain with respect to the non-swelling one. As a result, a helical ribbon with its ridges parallel to the helical axis forms. This constraint leads to a unique β for a given α that, in turn, is employed to determine the radius r *via* eqn (1); λ, T_V, and α are experimental parameters.

Our experimental observations are largely explained by the simple geometric model described above. Fig. 2(b) and (c) show that ridges indeed align almost parallel to the helical axes of the ribbons when the non-swelling parylene-C film is deposited on the topographically patterned side (see Fig. S4 in ESI† for other images, including a control experiment using a strip without topography). Geometrically, this behaviour follows because the parylene can only bend in one direction in order to maintain a vanishing Gaussian curvature. Any other orientation of the ridges would require the parylene to curve in two directions to conform with the topography. Besides the ridge orientations, the radii of the helical ribbons without self-interaction agree with model predictions when the effective swelling ratio, $\lambda \sim 1.07$, instead of 1.14 measured for unbounded PDMS.[53] It is reasonable, however, that the estimated effective swelling ratio is smaller than the unbounded case, because the strongly attached parylene layer suppresses swelling of PDMS compared to unbounded PDMS.[54,55]

The simple model provides a very useful first estimate of what happens to the film, but the model has limitations. For example, when the pitch is smaller than the width, W, of the ribbon, then the helical ribbon starts to interact with itself. An extreme example of this situation is the tube-like structure shown in Fig. 2(c); it cannot have constant r and β, because the ribbon needs to wrap around itself. Similarly, the helical ribbon can form a closed tubule where r and β are different from the ones with minimal stress/strain of the bilayer according to the geometric model. Additionally, the assumption of zero Gaussian curvature of the swollen structure is not strictly true; the assumption is based on the notion that the area of the non-swelling parylene-C film does not change. Since the parylene-C film is at least 100 times thinner than the PDMS (although its Young's modulus is 3 orders of magnitude greater than that of PDMS), it is possible that parylene-C is slightly stretched by the

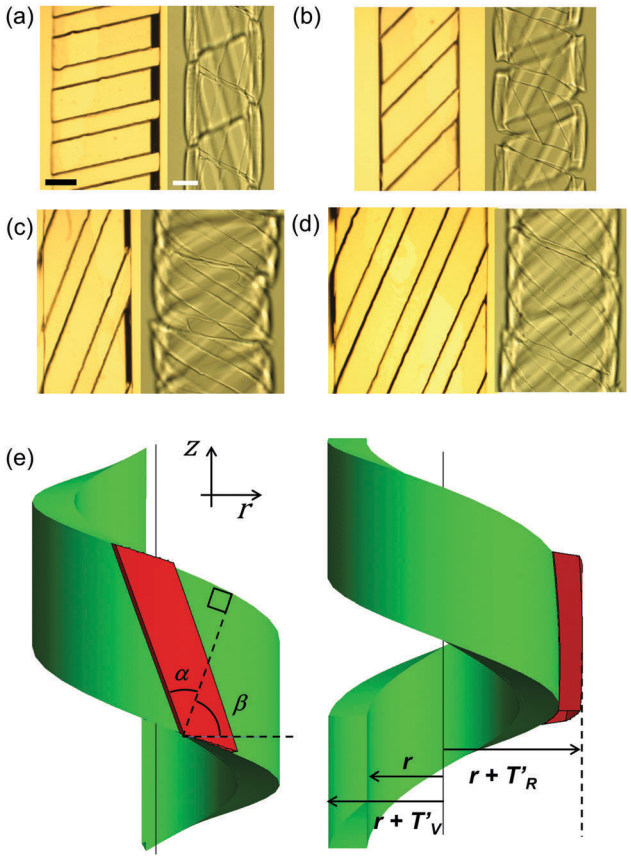

Fig. 4 Bilayer strips with parylene-C film deposited on the flat side of the patterned PDMS. (a–d) Optical microscopy images of bilayer strips in the dry (left) and swollen states (right), respectively. Swollen strips are in hexadecane. Scale bars: 100 μm. (e) 3D perspective views of a helical ribbon after swelling. For clarity, only one representative ridge is shown.

swelling of PDMS. In fact, even in the helical ribbon with ridges parallel to the helical axes, the parylene-C film on the ridges and valleys could be slightly stretched or compressed along the width-direction, since they have different radii of curvatures, r-T_V' and r-T_R'. Lastly, any residual stress from the deposited thin film (compressive or tensile) is not taken into consideration by the simple model; this effect is equivalent to an offset stress and can also affect the radii of curvature.

When parylene-C is deposited on the flat side of the patterned PDMS film, the swollen films again evolve into helical structures. As shown in Fig. 4, the ridges are now located at the outside of the helical ribbon. They are no longer parallel to the helical axis, and they exhibit specific angles that vary according to the geometry of the strip, *e.g.*, the width and the relative angle of the ridges.

We adopt the same simple geometric model of the helical ribbon to qualitatively explain the buckling. Again, we assume that the length of the PDMS strip, L_{out}, expands to match λL:

$$L_{out} = L\sqrt{\sin^2\left(\frac{\pi}{2}-\beta\right) + \left(\frac{r+T_V'}{r}\cos\left(\frac{\pi}{2}-\beta\right)\right)^2} = \lambda L. \quad (3)$$

Because the parylene-C film is deposited on the flat side of the PDMS film it does not constrain lengths on the topographically patterned side of the film and the length of ridges located outside of the helical ribbon, $L_{R,out}$, will swell to match λL_R.

$$L_{R,out} = L_R\sqrt{\sin^2(\alpha+\beta) + \left(\frac{r+T_R'}{r}\cos(\alpha+\beta)\right)^2} = \lambda L_R. \quad (4)$$

For a given strip dimension and swelling ratio, we often find that two sets of solutions, r and β, satisfy eqn (3) and (4) (see Fig. S5 in ESI†).

Thus, in this case, the simple analytic model does not uniquely explain the experimental observations of the bilayer film buckling. Nevertheless, if we assume that the solution for a larger tube diameter has the smaller deformation energy (and we select this solution among the two options), then we obtain shapes that are relatively close to the experimental observation (see Fig. S5 in ESI†). Of course, as noted above, this approach offers only a first estimate since the predictions are pure geometric solutions without energetic considerations. The simple argument considers only swelling along the length-direction of the strip and ridges, assumes zero Gaussian curvature, and neglects deformations along the width-direction and any internal strain within the strip. Moreover, as shown in Fig. 4(a), (c), and (d), self-interaction within the buckled strip will play a major role in cases of closed helical tubules, where friction within the structures and mechanical energetics determine the final configurations. To fully understand and predict the swollen structures for more of these varied situations, numerical analysis will be essential, which is beyond the scope of the simple geometric model.

Conclusions

We have demonstrated and elucidated the use of surface topography to guide swelling-induced buckling of a PDMS/parylene-C bilayer film. A non-swelling overlayer of a material with higher stretching stiffness imposes a constraint in the buckling of this class of bilayer film. The topographic pattern guides buckling by adding another constraint: the film deposited on the pattern will seek to minimize area changes. Non-swelling stiff films on stripe patterns, for example, evolve so that the stripes align parallel to the direction of zero curvature of the buckled 3D structure. The stiff and non-swelling parylene-C deposited on the topographically patterned side of the PDMS film causes the bilayer strip to form helical ribbons of almost zero Gaussian curvature with ridges/valleys of PDMS aligned parallel to the helical axis. When parylene-C is deposited on the flat side of PDMS film, the Gaussian curvature still vanishes and now the buckling causes the unconstrained ridges/valleys to have different radii of curvature due to the difference in thickness. Qualitatively, the helical ribbons formed choose a specific helix angle and radius to best match the swollen dimensions of ridges and valleys.

Looking forward, our theoretical understanding about the role of surface topography in buckling induced 3D structures could be improved, for example, by considering other deformations including internal strain and by relaxing assumptions

about zero Gaussian curvature. Nevertheless, the simple model gives the first-step guidance for application of the topography concept, and our work shows that approximate morphologies can be inferred from physical constraints. Of course minimization of the total elastic energy and avoid of self-interaction can be a critical factor in the determination of the final structure; the transforming objects can also become trapped into metastable structures formed along the buckling pathway.

Despite these limitations, we have shown that control of the surface topography on 2D sheets offers a rich and simple method to pre-program the buckling toward desired 3D objects, *e.g.* with a preferred curvature and/or direction of buckling. Furthermore, because topography can be easily incorporated utilizing various soft lithography techniques, our method is compatible with established strategies such as multi-layering and in-plane patterning that could further induce symmetry breaking[56] and facilitate the buckling process. Finally, we speculate that nature might also employ topographic patterning for facilitation of deformation and response. Natural structures with surface topography are ubiquitous in geological strata and morphogenesis of plants and animals;[57,58] interestingly, topographic patterns often arise from mechanical instabilities such as wrinkling and folding, which are local buckling modes. Thus, topography may play key roles when whole structures respond to external stresses and deform.

Acknowledgements

Authors gratefully acknowledge financial support from the National Science Foundation through DMR-1205463, DMR-1262047, DMR-1120901 (*i.e.*, the Penn MRSEC and its optical microscopy SEF), and Emerging Frontiers in Research and Innovation-Origami Design for Integration of Self-Assembling Systems for Engineering Innovation (NSF/EFRI-ODISSEI) Grant, #EFRI 13-31583. A. G. Y. acknowledges partial support from NASA through grant #NNX08AO0G. J. J. acknowledges support from the Korean Government through NRF-2015R1A2A2A01007613 and IBS-R020-D1. This work is also supported by a Simons Investigator grant from the Simons Foundation to R. D. K.

Notes and references

1 M. Marder, R. D. Deegan and E. Sharon, *Phys. Today*, 2007, **60**, 33–38.
2 L. Ionov, *Soft Matter*, 2011, **7**, 6786.
3 L. Ionov, *Adv. Funct. Mater.*, 2013, **23**, 4555–4570.
4 R. Kempaiah and Z. Nie, *J. Mater. Chem. B*, 2014, **2**, 2357.
5 A. R. Studart and R. M. Erb, *Soft Matter*, 2014, **10**, 1284–1294.
6 R. Geryak and V. V. Tsukruk, *Soft Matter*, 2014, **10**, 1246–1263.
7 D. Chen, J. Yoon, D. Chandra, A. J. Crosby and R. C. Hayward, *J. Polym. Sci., Part B: Polym. Phys.*, 2014, **52**, 1441–1461.
8 K. Krieger, *Nature*, 2012, **488**, 146–147.
9 C. Py, P. Reverdy, L. Doppler, J. Bico, B. Roman and C. N. Baroud, *Phys. Rev. Lett.*, 2007, **98**, 156103.
10 T. G. Leong, P. A. Lester, T. L. Koh, E. K. Call and D. H. Gracias, *Langmuir*, 2007, **23**, 8747–8751.
11 T. G. Leong, B. R. Benson, E. K. Call and D. H. Gracias, *Small*, 2008, **4**, 1605–1609.
12 X. Guo, H. Li, B. Yeop Ahn, E. B. Duoss, K. J. Hsia, J. A. Lewis and R. G. Nuzzo, *Proc. Natl. Acad. Sci. U. S. A.*, 2009, **106**, 20149–20154.
13 T. S. Shim, S.-H. H. Kim, C.-J. J. Heo, H. C. Jeon and S.-M. Yang, *Angew. Chem., Int. Ed.*, 2012, **51**, 1420–1423.
14 J. Kim, J. A. Hanna, M. Byun, C. D. Santangelo and R. C. Hayward, *Science*, 2012, **335**, 1201–1205.
15 J. Kim, J. A. Hanna, R. C. Hayward and C. D. Santangelo, *Soft Matter*, 2012, **8**, 2375.
16 M. Byun, C. D. Santangelo and R. C. Hayward, *Soft Matter*, 2013, **9**, 8264.
17 T. Castle, Y. Cho, X. Gong, E. Jung, D. M. Sussman, S. Yang and R. D. Kamien, *Phys. Rev. Lett.*, 2014, **113**, 245502.
18 Y. Cho, J.-H. Shin, A. Costa, T. A. Kim, V. Kunin, J. Li, S. Y. Lee, S. Yang, H. N. Han, I.-S. Choi and D. J. Srolovitz, *Proc. Natl. Acad. Sci. U. S. A.*, 2014, **111**, 17390–17395.
19 J.-H. Na, A. A. Evans, J. Bae, M. C. Chiappelli, C. D. Santangelo, R. J. Lang, T. C. Hull and R. C. Hayward, *Adv. Mater.*, 2015, **27**, 79–85.
20 J. Ryu, M. D'Amato, X. Cui, K. N. Long, H. Jerry Qi and M. L. Dunn, *Appl. Phys. Lett.*, 2012, **100**, 161908.
21 Y. Liu, J. K. Boyles, J. Genzer and M. D. Dickey, *Soft Matter*, 2012, **8**, 1764.
22 A. Sydney Gladman, E. A. Matsumoto, R. G. Nuzzo, L. Mahadevan and J. A. Lewis, *Nat. Mater.*, 2016, **15**, 413–418.
23 Q. Ge, H. J. Qi and M. L. Dunn, *Appl. Phys. Lett.*, 2013, **103**, 131901.
24 E. Smela, O. Inganäs and I. Lundström, *Science*, 1995, **268**, 1735–1738.
25 G. M. Whitesides, N. Bowden, S. Brittain, A. G. Evans and J. W. Hutchinson, *Nature*, 1998, **393**, 146–149.
26 Y. Yu, M. Nakano and T. Ikeda, *Nature*, 2003, **425**, 145.
27 M. Camacho-Lopez, H. Finkelmann, P. Palffy-Muhoray and M. Shelley, *Nat. Mater.*, 2004, **3**, 307–310.
28 P. D. Topham, J. R. Howse, C. J. Crook, S. P. Armes, R. A. L. Jones and A. J. Ryan, *Macromolecules*, 2007, **40**, 4393–4395.
29 E. Sultan and A. Boudaoud, *J. Appl. Mech.*, 2008, **75**, 51002.
30 J. M. G. Swann and A. J. Ryan, *Polym. Int.*, 2009, **58**, 285–289.
31 Z. Chen, C. Majidi, D. J. Srolovitz and M. Haataja, *Appl. Phys. Lett.*, 2011, **98**, 19–22.
32 M. Jamal, A. M. Zarafshar and D. H. Gracias, *Nat. Commun.*, 2011, **2**, 527.
33 J. Huang, J. Liu, B. Kroll, K. Bertoldi and D. R. Clarke, *Soft Matter*, 2012, **8**, 6291.
34 Z. L. Wu, M. Moshe, J. Greener, H. Therien-Aubin, Z. Nie, E. Sharon and E. Kumacheva, *Nat. Commun.*, 2013, **4**, 1586.
35 M. E. McConney, A. Martinez, V. P. Tondiglia, K. M. Lee, D. Langley, I. I. Smalyukh and T. J. White, *Adv. Mater.*, 2013, **25**, 5880–5885.
36 H. Thérien-Aubin, Z. L. Wu, Z. Nie and E. Kumacheva, *J. Am. Chem. Soc.*, 2013, **135**, 4834–4839.

37 Z. Hu, X. Zhang and Y. Li, *Science*, 1995, **269**, 525–527.
38 G. Stoychev, S. Zakharchenko, S. Turcaud, J. W. C. Dunlop and L. Ionov, *ACS Nano*, 2012, **6**, 3925–3934.
39 G. Stoychev, S. Turcaud, J. W. C. Dunlop and L. Ionov, *Adv. Funct. Mater.*, 2013, **23**, 2295–2300.
40 Y. Klein, E. Efrati and E. Sharon, *Science*, 2007, **315**, 1116–1120.
41 J. Kim, J. Yoon and R. C. Hayward, *Nat. Mater.*, 2010, **9**, 159–164.
42 W. T. S. Huck, N. Bowden, P. Onck, T. Pardoen, J. W. Hutchinson and G. M. Whitesides, *Langmuir*, 2000, **16**, 3497–3501.
43 D. S. Chung, G. B. Benedek, F. M. Konikoff and J. M. Donovan, *Proc. Natl. Acad. Sci. U. S. A.*, 1993, **90**, 11341–11345.
44 R. Oda, I. Huc, M. Schmutz, S. J. Candau and F. C. MacKintosh, *Nature*, 1999, **399**, 566–569.
45 J. T. Pham, J. Lawrence, D. Y. Lee, G. M. Grason, T. Emrick and A. J. Crosby, *Adv. Mater.*, 2013, **25**, 6703–6708.
46 M. Huang, C. Boone, M. Roberts, D. E. Savage, M. G. Lagally, N. Shaji, H. Qin, R. Blick, J. A. Nairn and F. Liu, *Adv. Mater.*, 2005, **17**, 2860–2864.
47 S. Douezan, M. Wyart, F. Brochard-Wyart and D. Cuvelier, *Soft Matter*, 2011, **7**, 1506.
48 Q. Guo, Z. Chen, W. Li, P. Dai, K. Ren, J. Lin, L. A. Taber and W. Chen, *EPL*, 2014, **105**, 64005.
49 Q. Guo, A. K. Mehta, M. A. Grover, W. Chen, D. G. Lynn and Z. Chen, *Appl. Phys. Lett.*, 2014, **104**, 211901.
50 S. Armon, E. Efrati, R. Kupferman and E. Sharon, *Science*, 2011, **333**, 1726–1729.
51 H.-S. Noh, K.-S. Moon, A. Cannon, P. J. Hesketh and C. P. Wong, *J. Micromech. Microeng.*, 2004, **14**, 625–631.
52 I. D. Johnston, D. K. McCluskey, C. K. L. Tan and M. C. Tracey, *J. Micromech. Microeng.*, 2014, **24**, 35017.
53 R. Dangla, F. Gallaire and C. N. Baroud, *Lab Chip*, 2010, **10**, 2972–2978.
54 M. E. Harmon, T. A. M. Jakob, W. Knoll and C. W. Frank, *Macromolecules*, 2002, **35**, 5999–6004.
55 R. Toomey, D. Freidank and J. Rühe, *Macromolecules*, 2004, **37**, 882–887.
56 B. Cao, G. Wu, Y. Xia and S. Yang, *Extrem. Mech. Lett.*, 2016, **7**, 49–54.
57 A. E. Shyer, T. Tallinen, N. L. Nerurkar, Z. Wei, E. S. Gil, D. L. Kaplan, C. J. Tabin and L. Mahadevan, *Science*, 2013, **342**, 212–218.
58 A. K. Harris, D. Stopak and P. Warner, *J. Embryol. Exp. Morphol.*, 1984, **80**, 1–20.

